Electronic Supplementary Information

Intrinsic high water/ion selectivity of graphene oxide lamellar membranes in concentration gradient-driven diffusion

Pengzhan Sun,[1,2] Renzhi Ma,[2*] Hui Deng,[1] Zhigong Song,[3,4] Zhen Zhen,[1,4] Kunlin Wang,[1]
Takayoshi Sasaki,[2] Zhiping Xu,[3,4*] Hongwei Zhu[1,4*]

[1]State Key Laboratory of New Ceramics and Fine Processing, School of Materials Science and Engineering, Tsinghua University, Beijing 100084, China
[2]International Center for Materials Nanoarchitectonics (WPI-MANA), National Institute for Materials Science (NIMS), 1-1 Namiki, Tsukuba, Ibaraki 305-0044, Japan
[3]Department of Engineering Mechanics, Tsinghua University, Beijing 100084, China
[4]Center for Nano and Micro Mechanics (CNMM), Tsinghua University, Beijing 100084, China

*Corresponding authors. Emails: MA.Renzhi@nims.go.jp; xuzp@tsinghua.edu.cn; hongweizhu@tsinghua.edu.cn.

This PDF file includes:

1. Materials and Methods
2. Supplementary Text
3. Figs. S1 to S11
4. References

1. Materials and Methods

1.1 Preparation of graphene oxide lamellar membranes (GOLMs)

Natural graphite was used for the preparation of graphite oxide by the modified Hummers' method (*1*), which was exposed to potassium permanganate, sodium nitrite and concentrated sulfuric acid for oxidation. The obtained graphite oxide flakes were exfoliated in water by vigorous sonication to yield graphene oxide (GO) nanosheets (*2-4*). Fig. S1A shows the atomic force microscopy (AFM) image of the as-synthesized GO nanosheets with a photograph of the corresponding aqueous suspension. The obtained GO nanosheets possessed a lateral dimension on the order of ~1 μm and a monolayer thickness of ~1 nm, which could be homogeneously dispersed in water to form a stable suspension. With the brown-colored GO aqueous suspension, GOLMs could be readily prepared by vacuum-assisted filtering through microfilters (*e.g.* polyvinylidene fluoride (PVDF) filter papers and anodized aluminium oxide (AAO) discs) (*5*, *6*), as shown in Figs. 1A, B (bottom insets). The PVDF filter papers possessed a diameter of ~47 mm, a pore size of ~0.2 μm and a thickness of ~100 μm, while the AAO discs possessed a diameter of ~25 mm, a pore size of ~0.2 μm and a thickness of ~50 μm. The interlayer spacing of the as-prepared GOLM was characterized by X-ray diffraction (XRD) in dry and fully wet states respectively in Fig. S1B. By immersing the GOLM in water, the interlayer spacing dramatically increased from ~0.78 to ~1.32 nm, yielding a void space of ~0.97 nm (1.32 – 0.35 nm, 0.35 nm is the distance of electronic clouds around graphene sheets) in GO interlayer galleries (*i.e.* sp^2 nanocapillaries) that was responsible for solution-based mass transport. Figs. S1C, D show the scanning electron microscopy (SEM) characterizations for the morphologies of micron- and several hundred nanometer-thick GOLMs, revealing that both the as-prepared membranes were continuous with wrinkles decorated.

1.2 Experimental setups

***Concentration gradient-driven diffusion*:** The concentration gradient-driven transmembrane diffusion experiments were performed with a self-made permeation apparatus, which was composed of a feed reservoir and a permeate reservoir separated by a plastic plate with a leak hole in the center (diameter: 5 mm). A piece of GOLM (on PVDF microfilter) was sealed with double-sided copper tape that was drilled with the same sized hole so that the membrane could directly connect the feed and permeate solutions and facilitate transmembrane permeation. In order to extract the effect of PVDF support, control experiments were conducted using bare microfilters with all other steps remaining the same. Note that the double-sided copper tapes could provide excellent seal for the transmembrane permeation experiments, which was confirmed by the absence of any detectable permeations lasting for several days through the leak hole sealed with an entire piece of double-sided coper tape instead of a permeable membrane (*e.g.* GOLM on microfilter or bare microfilter).

In a typical experiment, equivalent volumes (150 mL) of certain salt solution (0.1 M in concentration unless otherwise mentioned) and deionized water were injected at the same speed into the feed and permeate reservoirs, respectively. Mild magnetic stirrings were applied to the feed and permeate solutions to eliminate the concentration polarization effect. The water permeation was investigated based on an isotope labelling technique, in which certain amount of deuterium oxide (D_2O) was dissolved into the feed solution as a tracer. The transmembrane permeance of D_2O was monitored with time by attenuated total reflection Flourier transformed infrared spectroscopy (ATR-FTIR) to extrapolate that of water. Simultaneously, the conductivity of the permeate solution was measured with time for calculating and plotting the salt permeance as a function of time according to the fact that in a dilute salt solution the conductivity varies linearly with concentration.

Specially, for measuring the pH-dependent water and ion transmembrane permeations, the pH values of the 0.1 M KCl feed solutions were adjusted with HCl or KOH, and the K^+ or Cl^- concentrations in permeate solutions were measured by inductively coupled plasma atomic emission spectroscopy or ion chromatography, respectively. Fig. 1 (top inset) and Figs. S2A, B show the schematic diagram and corresponding photographs for the transmembrane diffusion experimental setups.

***Pressure-driven filtration*:** The pressure-driven filtration experiments were performed by sealing

GOLM (on AAO) with O-rings in a dead end filtration device pressurized with N_2 gas flow, as illustrated in Fig. 4 (top inset). A photograph of the pressurized filtration device is shown in Fig. S2C. In a typical experiment, 100 mL of a certain feed solution was injected into the chamber from Valve 1 with Valve 2 opened for balancing the internal pressure (Fig. S2C). Then Valve 1 and Valve 2 were closed and N_2 gas flow was introduced for applying pressure. The feed solution was allowed to percolate through GOLM under a pressure of 0.1 MPa. The corresponding permeate solution was collected with time for measuring the flux and salt rejection rate ($R = 1 - c_p/c_f$, where R is rejection rate, c_p and c_f are concentrations of the permeate and feed solutions, respectively).

Selection of microfilters**:** For concentration gradient-driven diffusion experiments, PVDF filter papers were used for vacuum-assisted preparing GOLMs due to the characteristics of being flexible and easy to deform that were beneficial for excellent seal with double-sided copper tapes. However, for pressure-driven filtration experiments, we found that the common swelling effect of polymeric microfilters in water caused serious corrugations under pressure, further giving rise to large tears in GOLMs with serious leakage. Therefore, AAO discs with flat surface and rigidity were used instead in pressurized filtration experiments. According to a recent study (*7*), despite the different kinds of microfilters used, as-prepared GOLMs possessed the same lamellar structure and interlayer spacing. Considering that the several hundred nanometer-thick GOLM could be prepared by vacuum-filtering extremely dilute GO suspension through AAO disc within several tens of minutes, the corrosion of AAO and the cross-linking of GOLM by the released Al^{3+} ions could be neglected. Therefore, it was believed that the GOLMs prepared on PVDF papers and AAO discs possessed no substantial differences and the results obtained in diffusion and pressurized filtration with GOLMs on different microfilters reflected their intrinsic mass transport properties.

1.3 Molecular dynamics (MD) simulations

Molecular models and simulation details**:** The molecular structure of GO consisted of hydroxyl, epoxy and carbonyl groups on the basal plane. Hydroxyl groups had been reported to be able to stay rich in the long-living quasi-equilibrium state (*8*) and thus were focused on in this work, although our additional simulations showed that epoxy groups had similar effects on the water flow. A typical fraction of hydroxyl species relative to the amount of carbon atoms in GO was ~ 20% (*8*), and further reduction could yield a lower concentration (13.9-15.9%) in reduced GO (RGO) (*9*). For oxidized regions of GO, we constructed hydroxyl-functionalized graphene on both sides of the sheet with concentration $c = n_{OH}/n_C = 20\%$ in this study, where n_{OH} and n_C are number densities of hydroxyl groups and carbon atoms, respectively. The distribution of hydroxyl groups was sampled randomly in the oxidized region.

We constructed squared two-dimensional GO platelets by using periodic boundary conditions (PBCs) with lateral dimensions of 20.022 and 19.894 nm, respectively. The thickness of interlayer GO channel was 1.32 nm, consistent with the XRD characterizations in Fig. S1B, which was filled with 0.1 M KCl aqueous solution.

We performed MD simulations using the large-scale atomic/molecular massively parallel simulator (LAMMPS) (*10*). The all-atom optimized potential for liquid simulations (OPLS-AA) was used for GO platelets and KCl aqueous solution, which could capture essential many-body terms in inter-atomic interactions, including bond stretching, bond angle bending, van der Waals and electrostatic interactions (*11*). Following the previous studies on similar systems (*12-15*), the extended simple point charge model (SPC/E) was used for water molecules due to its predictability of dynamical properties such as viscosity. The SHAKE algorithm was applied for the stretching bond terms between oxygen and hydrogen atoms to reduce high-frequency vibrations that required shorter time steps. The interactions between water and functional groups included both van der Waals and electrostatic terms. The former one was described by the 12-6 Lennard-Jones potential $4\varepsilon[(\sigma/r)12 - (\sigma/r)6]$ between oxygen and carbon atoms with parameters $\varepsilon_{C\text{-}O} = 4.059$ meV, $\sigma_{C\text{-}O} = 0.319$ nm, $\varepsilon_{C\text{-}C(\text{-}H)} = 3.048$ meV, $\sigma_{C\text{-}C(\text{-}H)} = 0.355$ nm, $\varepsilon_{C\text{-}C(\text{-}OH)} = 3.048$ meV, $\sigma_{C\text{-}C(\text{-}OH)} = 0.355$ nm, and $\varepsilon_{O\text{-}O(\text{-}OH)} = 6.721$ meV, $\sigma_{O\text{-}O(\text{-}OH)} = 0.307$ nm at an inter-atomic distance r (*16*). In the functional groups, atomic charges were set as follows: $q_{C(\text{-}H)} = -0.2000$, $q_{H(\text{-}H)} = 0.2000$, $q_{C(\text{-}OH)} = 0.2000$, $q_{O(\text{-}OH)} = -0.6400$, $q_{H(\text{-}OH)} = 0.4400$ (*17*). The van der Waals forces were truncated at 1.2 nm and the long-range Coulomb interactions were computed by using the particle-particle particle-mesh

(PPPM) algorithm (*18*). The cations and anions were added in a way to maintain the charge neutrality. The time step of equation of motion integration was 2 fs. For temperature and pressure controls, we used the Nosé-Hoover thermostat and Berendsen barostat, respectively.

***Pressure-induced flow and diffusion*:** Pressure-induced flow was obtained from the applied pressure gradient along the GO channel by adding pre-assigned force parallel to the channel on every water molecule, K^+ ion and Cl^- ion. The assigned rules were as follows:

$$M_{\mathrm{total}} = m_{\mathrm{water}} \times n_{\mathrm{water}} + m_{\mathrm{K}} \times n_{\mathrm{K}} + m_{\mathrm{Cl}} \times n_{\mathrm{Cl}}$$

$$f_{\mathrm{water}} = F/M_{\mathrm{total}} \times m_{\mathrm{water}}$$

$$f_{\mathrm{K}} = F/M_{\mathrm{total}} \times m_{\mathrm{K}}$$

$$f_{\mathrm{Cl}} = F/M_{\mathrm{total}} \times m_{\mathrm{Cl}}$$

where n_{X}, m_{X} and f_{X} (X = water, K and Cl) are the number, relative atomic mass and pre-assigned force of water molecules, K^+ ions and Cl^- ions, respectively. F is total force and M_{total} is total mass.

Consistent with diffusion simulations, the whole system was equilibrated at 300 K and 1 a.t.m for 5 ns before any data collection in order to achieve steady flow. Accumulated net flux and diffusive flux as long as 10 ns for water molecules, K^+ ions and Cl^- ions were compared under different pressure gradients.

***Mean residual time (MRT) of water in the solvation shell*:** To capture the molecular hydrodynamics of ion transport in pressure-induced flow, we extracted the MRT of water molecules in the first solvation shell around these ions from MD trajectories. The radius of first solvation shell around the central ion under investigation was deduced from the first peak of radial distribution function (RDF) between central ion and oxygen atom of surrounding water molecules. MRT distribution functions for water molecules around ion in the first solvation shell were calculated from $P(t) = N_{\mathrm{R}}(t, \Delta t)/\Sigma_t N_{\mathrm{R}}(t, \Delta t)$, where $N_{\mathrm{R}}(t, \Delta t)$ is the number of water molecules around the ion in the first solvation shell that (i) remained unperturbed at times up to $t \pm \Delta t/2$ and (ii) were broken at $t \pm \Delta t$. $N_{\mathrm{R}}(t, \Delta t)$ was calculated through sampling of every time origin, Δt was set to 10 fs, and the MRT was calculated through the ensemble average, $\tau_{\mathrm{R}} = \Sigma_t tP(t)$.

***Steered molecular dynamics (SMD) simulations*:** To understand the different transport mechanisms between water molecules and ions (K^+ and Cl^-) travelling into and out of GO channel, we performed SMD simulations to explore the free energy profiles for the diffusions of a water molecule, K^+ ion and Cl^- ion through GO channel. Here we established a model of finite 2 nm-long GO channel with hydroxyl edges, which was filled with pure water. The whole system was equilibrated at 300 K and 1 a.t.m. for 2 ns.

2. Supplementary Text

Calculation of D_2O and ion diffusivities through GOLM by extracting the effect of microfilter

Diffusivities of D_2O and salts through GOLM were calculated according to Fick's first law ($J = -D\Delta c/l$, where J is flux, D is diffusivity, Δc is concentration gradient and l is membrane thickness) by extracting the effect of microfilter, as illustrated in Fig. S3.

In detail, as shown in Fig. S3A, the diffusion through bare microfilter was expressed as follows:

$$J_{\mathrm{m}} = D_{\mathrm{m}} \frac{c_0 - c_1}{l_{\mathrm{m}}} \tag{1}$$

where the subscript m represents microfilter, c_0 and c_1 are concentrations of the feed and permeate solutions, respectively. During the 12 h-long diffusion processes, both the D_2O and salt concentration enhancements in the permeate solution could be neglected compared to the feed concentrations. Therefore, Eq. (1) was simplified as follows:

$$J_{\mathrm{m}} = D_{\mathrm{m}} \frac{c_0}{l_{\mathrm{m}}} \tag{2}$$

As shown in Fig. S3B, the diffusion through GOLM on microfilter was expressed as follows considering the equivalent fluxes through GOLM and the microfilter behind:

$$J_{\mathrm{g-m}} = D_{\mathrm{g}} \frac{c_0 - c_2}{l_{\mathrm{g}}} = D_{\mathrm{m}} \frac{c_2 - c_3}{l_{\mathrm{m}}} \tag{3}$$

where the subscripts g-m and g represent GOLM on microfilter and GOLM, respectively. c_2 is the concentration at the GOLM/microfilter interface, c_3 is the concentration of the permeate solution. Again, c_3 could be neglected compared to c_0 and c_2, and Eq. (3) was simplified as follows:

$$J_2 = D_{\mathrm{g}} \frac{c_0 - c_2}{l_{\mathrm{g}}} = D_{\mathrm{m}} \frac{c_2}{l_{\mathrm{m}}} \tag{4}$$

Combining Eqs. (2) and (4), one could calculate the diffusivities of D_2O and salts through GOLM.

Quantifying D_2O concentration by ATR-FTIR spectrum

Prior to the synchronous investigation on concentration gradient-driven water and salt diffusions by isotope labelling, the validity of quantifying D_2O concentration changes in permeate solutions by ATR-FTIR was confirmed. Fig. S4A shows a typical ATR-FTIR spectrum of 30 wt% D_2O in water, which has been baselined and normalized with the peak located at ~3400 cm^{-1}. Due to the slightly larger mass of D_2O than H_2O, the peaks assigned to extension vibration mode (v_1 and v_3) located at ~3400 cm^{-1} and angular vibration mode (v_2) located at ~1650 cm^{-1} in H_2O shifted to ~2500 cm^{-1} and ~1210 cm^{-1} respectively in D_2O. In Fig. S4B, the normalized absorption intensities at ~2500 cm^{-1} in the ATR-FTIR spectra (A_D) of D_2O in water were plotted as a function of D_2O concentration (c_D), revealing the excellent fit into a linear relationship: $A_D = 0.0305c_D$, based on which the concentration of D_2O in water could be determined and water transmembrane permeation could be further extrapolated.

Quantifying the permeation differences between D_2O and H_2O

Recently, Lozada-Hidalgo, *et al.* (*19*) reported that protons permeated through the two-dimensional crystals such as monolayers of graphene and boron nitride much faster than deuterons, with a separation factor of ~10 at room temperature, which could be attributed to a ~60 meV-difference between 0-point energies of incident protons and deuterons that translated into the activation barrier differences posed by graphene or boron nitride. This inspired us to quantify the possible differences between D_2O and H_2O when permeating through the nanochannels within GOLM. To achieve this, an experiment was designed as follows (illustrated in Fig. S5A): by injecting equivalent volumes of D_2O (99.9 % in purity) and deionized water into the feed and permeate reservoirs respectively separated by either GOLM on microfilter or bare microfilter, the permeations of D_2O (from feed to permeate) and H_2O (from permeate to feed) were monitored by ATR-FTIR simultaneously. The permeances of D_2O from feed to permeate as a function of time could be determined according to the linear absorption-concentration relationship in Fig. S4B. For the determination of H_2O permeations from permeate to feed, the ATR-FTIR spectra were firstly baselined and normalized with the peak assigned to D_2O at ~2500 cm^{-1}, and then the normalized absorption intensities at ~3400 cm^{-1} (A_H) were plotted as a function of H_2O concentration in D_2O (c_H), as shown in Fig. S5B, revealing a linear fit with a function relationship of $A_H = 0.0262c_H$. Figs. S5C, D show the representative normalized ATR-FTIR spectra of the feed and permeate solutions at various intervals during the permeations through microfilter and GOLM on microfilter respectively, revealing that the normalized absorption intensities of the peaks assigned to H_2O and D_2O in feed and permeate solutions respectively increased gradually with time. With these spectra and according to the linear absorption-concentration relationships in Figs. S4B and S5B, the permeances of D_2O (from feed to permeate) and H_2O (from permeate to feed) through microfilter and GOLM on microfilter could be calculated, as plotted in Figs. S5E, F. All the permeances increased linearly with time, the slops of which yielded the fluxes (*J*) of D_2O and H_2O through microfilter and GOLM on microfilter, respectively. The permeations of H_2O were faster than D_2O in both cases, possibly due to the larger mass of D_2O than H_2O. Notably, the deviation between the permeations of D_2O and H_2O in GOLM on microfilter case was more significant than that in bare microfilter case, indicating that the selectivity between H_2O and D_2O through the *sp*^{2} nanocapillaries in GOLM was greater than through the sub-micron-sized polymeric channels in microfilter.

The differences between the permeations of D_2O and H_2O through GOLM and microfilter were further quantified, based on which the permeations of H_2O could be precisely extrapolated. Firstly, the ratios between the fluxes of H_2O and D_2O through GOLM on microfilter and through microfilter could be calculated as follows:

$$\frac{J_{\mathrm{mH2O}}}{J_{\mathrm{mD2O}}} = 1.02 \tag{5}$$

$$\frac{J_{\mathrm{g-mH2O}}}{J_{\mathrm{g-mD2O}}} = 1.09 \tag{6}$$

According to Eqs. (5) and (6), the fluxes of H_2O through microfilter and GOLM on microfilter could be adjusted with those of D_2O.

Next, combining Eqs. (2) and (4), the ratios between the diffusivities of H_2O and D_2O through

GOLM and through microfilter could be calculated as follows:

$$\frac{D_{\mathrm{mH2O}}}{D_{\mathrm{mD2O}}} = \frac{J_{\mathrm{mH2O}}}{J_{\mathrm{mD2O}}} \times \frac{c_{\mathrm{0D2O}}}{c_{\mathrm{0H2O}}} = 1.02 \tag{7}$$

$$\frac{D_{\mathrm{gH2O}}}{D_{\mathrm{gD2O}}} = \frac{J_{\mathrm{g-mH2O}}}{J_{\mathrm{g-mD2O}}} \times \frac{c_{\mathrm{0D2O}}}{c_{\mathrm{0H2O}}} \times \frac{1-\frac{J_{\mathrm{g-mD2O}}}{J_{\mathrm{mD2O}}}}{1-\frac{J_{\mathrm{g-mH2O}}}{J_{\mathrm{mH2O}}}} = 1.39 \tag{8}$$

According to Eqs. (7) and (8), the diffusivities of H_2O through GOLM and microfilter could be adjusted with those of D_2O.

Determination of D_2O concentration for labelling feed solutions

Water sources labelled with various concentrations of D_2O were allowed to permeate through GOLM on microfilter, as shown in Fig. S6. The transmembrane permeation of pure D_2O (99.9% in purity) was included for comparison. The D_2O permeances increased linearly with time and a higher feed concentration generally resulted in a faster permeation rate. The transmembrane fluxes of D_2O were determined from the slops of the corresponding permeation curves (shown in Fig. S6A) and plotted as a function of D_2O feed concentration in Fig. S6B, revealing a linear relationship. This indicates that the diffusivity of D_2O through GOLM on microfilter was independent of its feed concentration according to Fick's first law ($J = -D\Delta c/l$, J varied linearly with Δc, l was a constant, so D was a constant). In the following isotope labelling-assisted concentration gradient-driven diffusion experiments, the concentration of D_2O tracers in feed solutions was chosen as 30 wt%.

Quantitative analysis of water and ion permeations through the nanochannels within GOLM

By considering the microstructures of GOLM and microfilter, water and salt permeations through the channels within these two kinds of membranes were evaluated according to the method proposed by Nair, *et al.* (*20*) and Joshi, *et al.* (*21*), which has been demonstrated to provide excellent matches with the experimental results and MD simulations.

In a GOLM with a thickness (t) of ~2.5 μm, thousands of GO nanosheets with a lateral dimension (l) of ~1 μm (Fig. S1A) were stacked together to form a lamellar structure. Mass transport mainly occurred through the interlayer galleries formed between adjacent GO nanosheets and leakage through the intrinsic defects within GO flakes could be neglected due to mutual stacking of thousands of layers, as illustrated in Fig. S9A. According to the XRD characterizations of GOLM in Fig. S1B, the interlayer spacing in the dry state (d) was ~0.78 nm, while that in the fully wet state was ~1.32 nm, giving rise to a critical nanochannel width (w) of ~1 nm (1.32 nm – 0.35 nm = 0.97 nm) for mass transport. The effective length of nanochannels across the whole stacking layers involving a total number of turns t/d could be evaluated as $L_{\mathrm{eff}} = lt/d \approx 3.2$ mm. Such ultralong and serpentine nanochannels only occupied a tiny portion of the whole membrane area, which could be estimated as $w/l \approx 0.1\%$, yielding an effective mass transport area of $A_{\mathrm{eff}} = Aw/l$. Therefore, the diffusivity through the nanochannels within GOLM could be estimated as $D_{\mathrm{channel}} = \frac{l^2}{wd} \times D \approx 1.3 \times 10^6 D$ according to the classical diffusion equation:

$$J = D \times \Delta c \times \frac{A}{t} = D_{\mathrm{channel}} \times \Delta c \times \frac{A_{\mathrm{eff}}}{L_{\mathrm{eff}}} = D_{\mathrm{channel}} \times \Delta c \times \frac{A}{t} \times \frac{wd}{l^2} \tag{9}$$

On the other hand, for microfilters, mass transport mainly occurred through the sub-micron-sized pores throughout the thickness. Considering the porosity of ~80% for a typical PVDF microfilter, the diffusivity through the pores within microfilter could be estimated as $D_{\mathrm{channel}} = \frac{1}{80\%} \times D \approx 1.3D$ according to Eq. (9). As shown in Fig. S8 and Fig. 2C, the diffusivities of various salts and corresponding solvent water through the entire GOLM were ~1 order of magnitude lower than through microfilter, based on which one could conclude that the diffusivities through the nanochannels within GOLM were roughly ~5 orders of magnitude greater than through the sub-micron-sized PVDF pores (*i.e.* the bulk diffusion cases). Note that this was a lower bound for the estimation of diffusivities through the nanochannels within GOLM because the oxygen-containing functional groups attached on graphene flakes were reported to suppress the permeations of water and salts (*14*, *15*).

In the above estimation, the leakage through the intrinsic defects (*e.g.* nanopores) was neglected due to mutual stacking of thousands of layers. In fact, according to recent high-resolution transmission electron microscopy (HRTEM) studies on GO flakes (*22-24*), the areal ratios of nanopores, sp^2 graphitic and sp^3 oxidized regions were roughly 2%, 16% and 82%, respectively. The nanopores on GO flakes occupied a tiny percentage that could be easily blocked by the adjacent impermeable oxidized regions upon stacking. As a critical case, the nanopores on GO flakes were assumed to be completely unblocked by the oxidized regions, acting as the role of shortening the nanochannels, as illustrated in Fig. S9B. For a ~1 μm-sized GO flake, the total area of nanpores could be calculated as ~0.02 μm^2, yielding a total lateral dimension of ~0.14 μm. Considering the permeability of small hydrated ions such as K^+, Na^+, Mg^{2+} and Ca^{2+}, the minimum dimension of nanopores on GO flakes that allowed mass transport should be >0.7 nm. This means that the micron-sized GO flake could be divided by <200 nanopores in ideal condition, shortening the effective length of nanochannels and further lowering the diffusivities by 2 orders of magnitude (the areal percentage of nanopores was tiny to change the effective mass transport area of GOLM). In addition, the length of a typical turn (t/d in total) involved in the serpentine nanochannel was assumed to be the average lateral dimension of GO nanosheets (~1 μm). Typically, this was slightly overestimated because the water molecules and ions would drop to the next void before gliding through the entire GO cross-section. As a critical case, no turns were assumed to be experienced by the permeations of water and ions through GOLM, as illustrated in Fig. S9C. The effective length of nanochannels could be significantly shortened to the thickness of GOLM and the diffusivities through the nanochannels could be lowered by 3 orders of magnitude without considering the related decrease in the effective mass transport area. In spite of the above ideal cases that are impossible in reality, the diffusivities through the nanochannels within GOLM were still 2-3 orders of magnitude greater than the bulk diffusion cases, showing the rapid mass transport properties of GOLM.

Steric hindrance effect and diverse interactions responsible for ion selectivity of GOLM

With GOLM, excellent selectivity could be achieved during the diffusions of various salts based on steric hindrance from sp^2 nanocapillaries, electrostatic and chemical interactions from the active sites on GOLM:

1) The comparable dimension of $Fe(CN)_6^{3-}$ (hydrated diameter: 0.95 nm) with the critical size of sp^2 nanocapillaries (~0.97 nm, Fig. S1B) and its high anion/cation valence ratio (Z^-/Z^+) gave rise to effective sieving of $K_3Fe(CN)_6$ by the steric hindrance from sp^2 nanocapillaries and

electrostatic repulsion from the ionized oxygen functionalities on GOLM (*e.g.* carboxyl);

2) Due to the higher negative charges of SO_4^{2-} than Cl^- associated with stronger electrostatic repulsion, the diffusions of SO_4^{2-}-salts (*e.g.* K_2SO_4 and $MgSO_4$) were generally slower than Cl^--salts (*e.g.* KCl and $MgCl_2$);

3) The anchoring originating from the cation-π interaction of K^+ with the sp^2 aromatic clusters on GO was much stronger than that of Na^+, resulting in slower diffusion of KCl than NaCl;

4) For Na^+ and Mg^{2+} ions, the higher positive charges of Mg^{2+} than Na^+ gave rise to stronger cation-π capture, resulting in slower diffusion of $MgCl_2$ than NaCl;

5) For Mg^{2+} and Ca^{2+} ions, the much smaller size of Mg^{2+} than Ca^{2+} associated with higher hydration energy resulted in sufficient water molecules being attached around Mg^{2+} to induce a strong screening to the cation-π interaction with the sp^2 aromatic clusters on GO, while Ca^{2+} was partially hydrated with a much weaker screening, further giving rise to slower diffusion of $CaCl_2$ than $MgCl_2$.

These results are in well agreement with the previous studies (*25*, *26*).

Formation of GOLM on microfilter with increasing GO coverage density and the corresponding ion transmembrane permeations

As shown in Fig. S10, the porous substrate was completely covered by GO nanosheets from 50.9 mg/m^2 and wrinkles began to emerge from 159.2 mg/m^2. On the other hand, the corresponding ion permeations (taking no account of the related water permeations) shown in Fig. S11 indicate that significant selectivity in ion fluxes was observed from 159.2 mg/m^2, implying the presence of large defects or discontinuity with serious leakage in thinner GOLMs. Notably, the tendency in ion selectivity exhibited an obvious transition with increasing the membrane thickness (*i.e.* GO nanochannel length). For the coverage densities of 159.2-318.3 mg/m^2, the flux of KCl was always higher than NaCl and the selectivity among various salts displayed a Z^-/Z^+-dependent tendency, indicative of electrostatic interaction as a major contributor to the ion selectivity of thinner GOLMs with more free sheet edges (*i.e.* short GO nanochannels). For the coverage densities of ≥636.6 mg/m^2, the flux of KCl became lower than NaCl and decreased sharply with increasing the membrane thickness. Considering the strong cation-π interaction between K^+ and the *sp*^{2} nanocapillaries, it could be concluded that for thicker GOLMs with more interlayer galleries (*i.e.* long GO nanochannels), the chemical interaction began to dominate the ion selectivity. Notably, the tendency in ion fluxes through GOLM with a coverage density of 318.3 mg/m^2 (Fig. S11E) was just opposite to that in rejections of GOLM with the same thickness in pressurized filtration (Fig. 5B). This indicates that the nanochannel length-correlated ion selectivity contributed substantially to the salt rejection of GOLM, while the ion-water interactions were seriously weakened in pressurized filtration, drawn from the independence of salt rejection on water effect, deviating from the diffusion case (Fig. 2D) and consistent with the MD simulations (Fig. 6).

3. Supplementary Figures

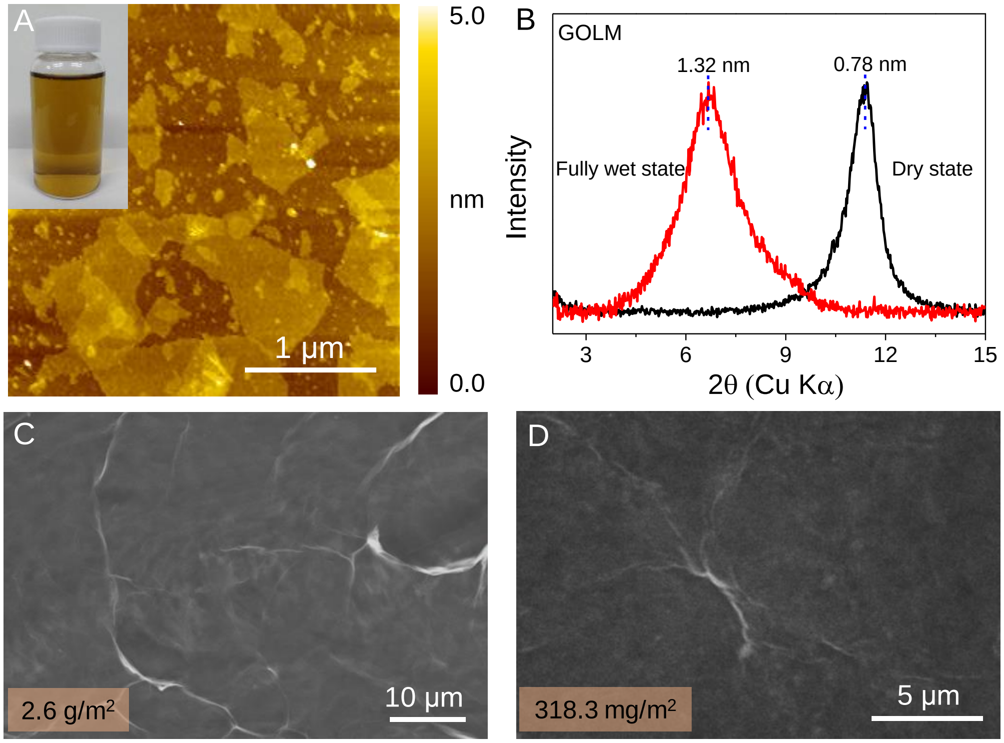

Fig. S1. (**A**) AFM image of GO nanosheets. Inset: the corresponding aqueous suspension. (**B**) XRD characterizations of GOLM. (**C**, **D**) SEM images of the morphologies of micron- and several hundred nanometer-thick GOLMs, respectively.

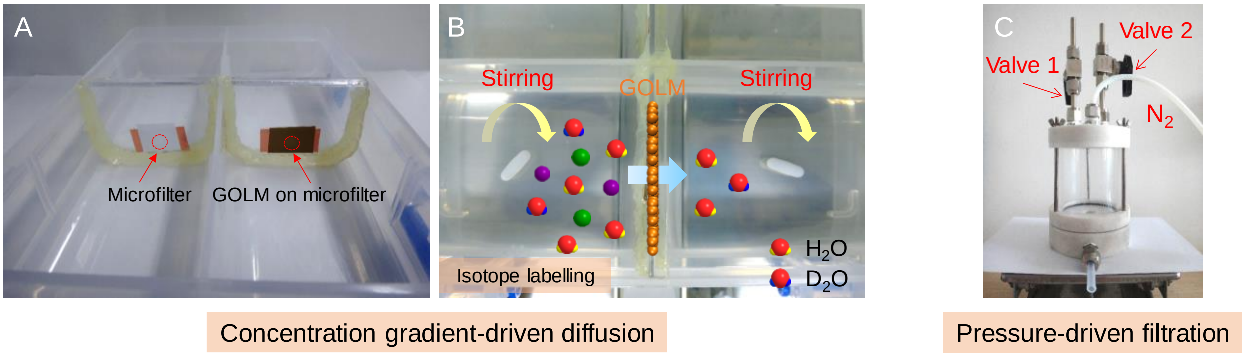

Fig. S2. Experimental setups for (**A**, **B**) concentration gradient-driven diffusion and (**C**) pressure-driven filtration.

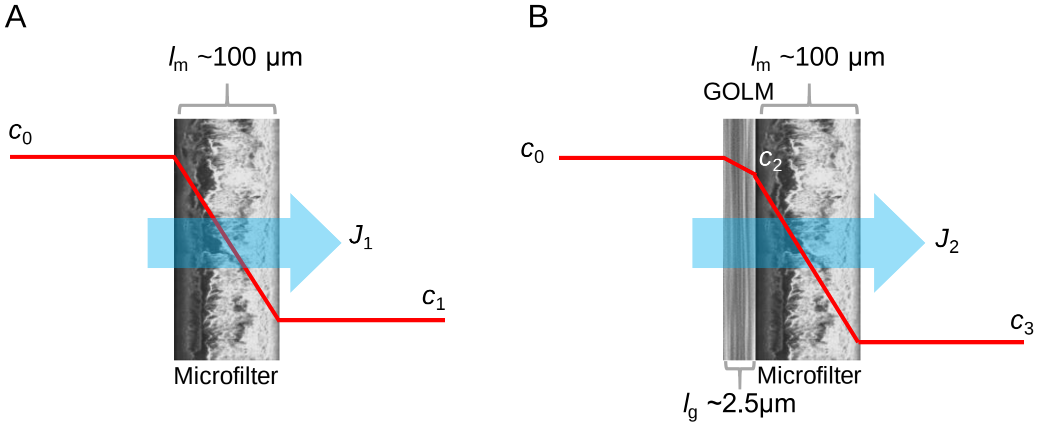

Fig. S3. Schematic diagrams for the calculation of diffusivities through GOLM by extracting the effect of microfilter. (**A**) Diffusion through bare microfilter. (**B**) Diffusion through GOLM on microfilter.

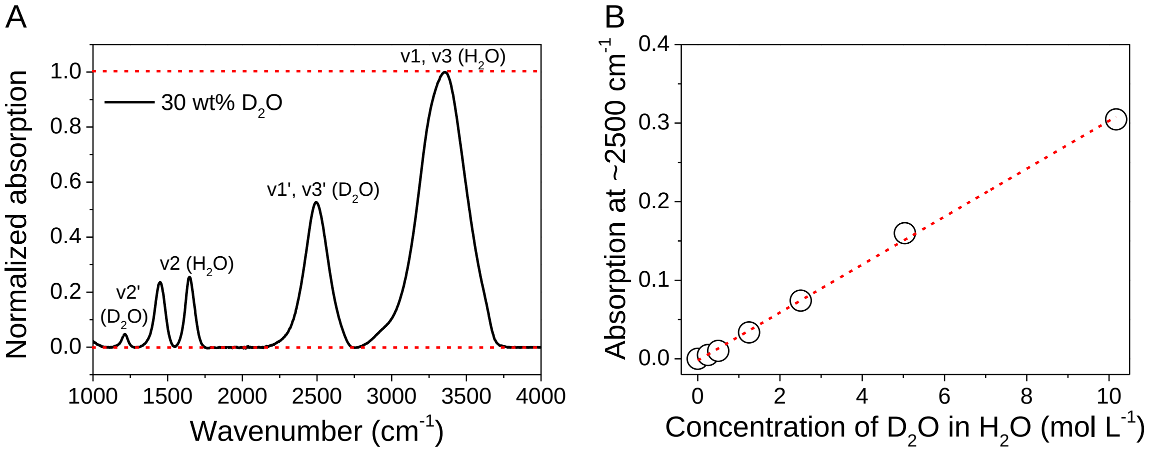

Fig. S4. (**A**) ATR-FTIR spectrum of 30 wt% D_2O in water. (**B**) Normalized absorption intensities at ~2500 cm^{-1} (by the intensities at ~3400 cm^{-1}) in ATR-FTIR spectra as a function of D_2O concentration in H_2O.

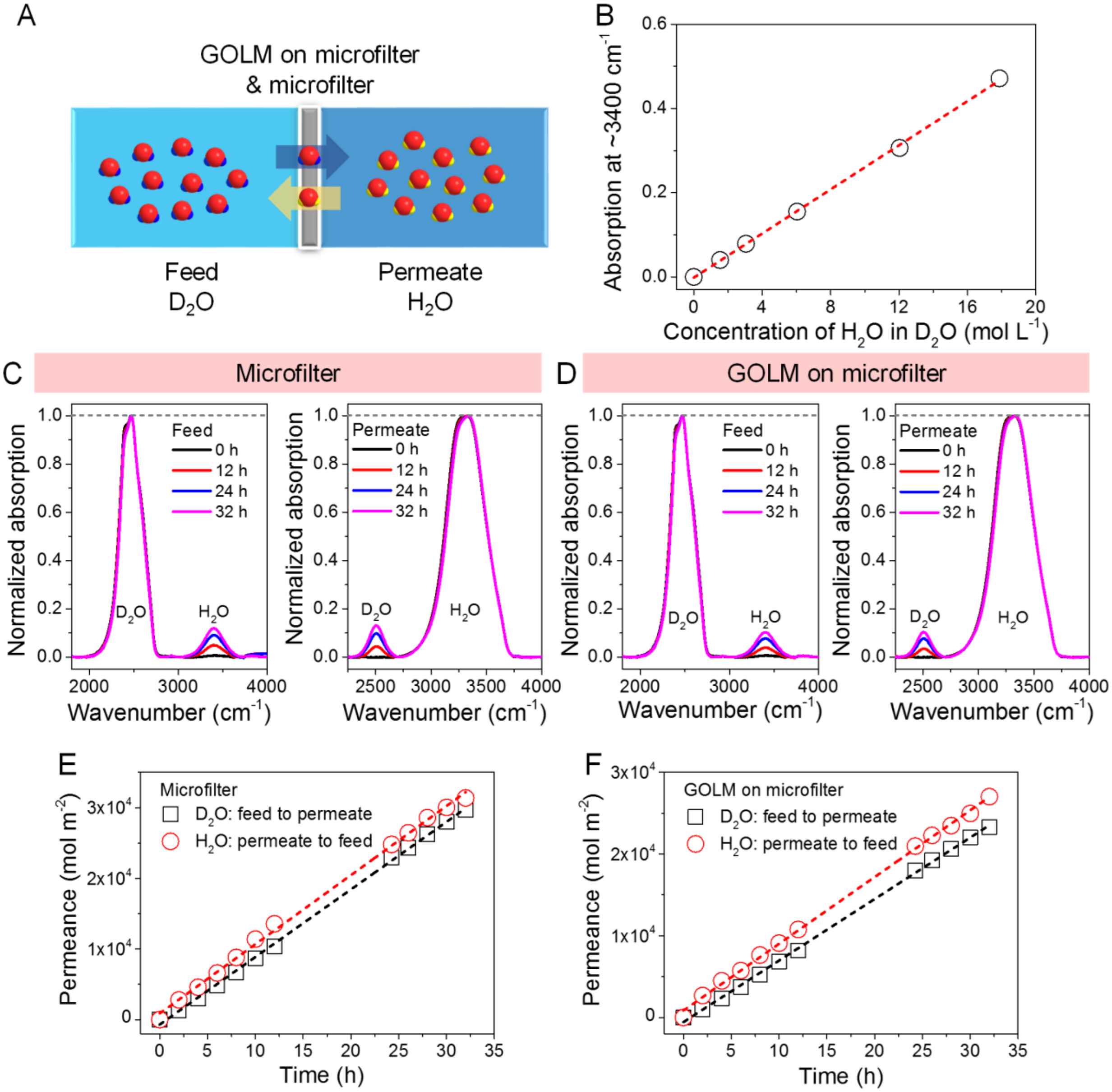

Fig. S5. (**A**) Schematic diagram for the experimental setup. (**B**) Normalized absorption intensities at ~3400 cm^{-1} (by the intensities at ~2500 cm^{-1}) in ATR-FTIR spectra as a function of H_2O concentration in D_2O. Representative ATR-FTIR spectra of the feed and permeate solutions at various intervals during the permeations through (**C**) microfilter and (**D**) GOLM on microfilter, respectively. The permeances of D_2O (from feed to permeate) and H_2O (from permeate to feed) as a function of time through (**E**) microfilter and (**F**) GOLM on microfilter, respectively.

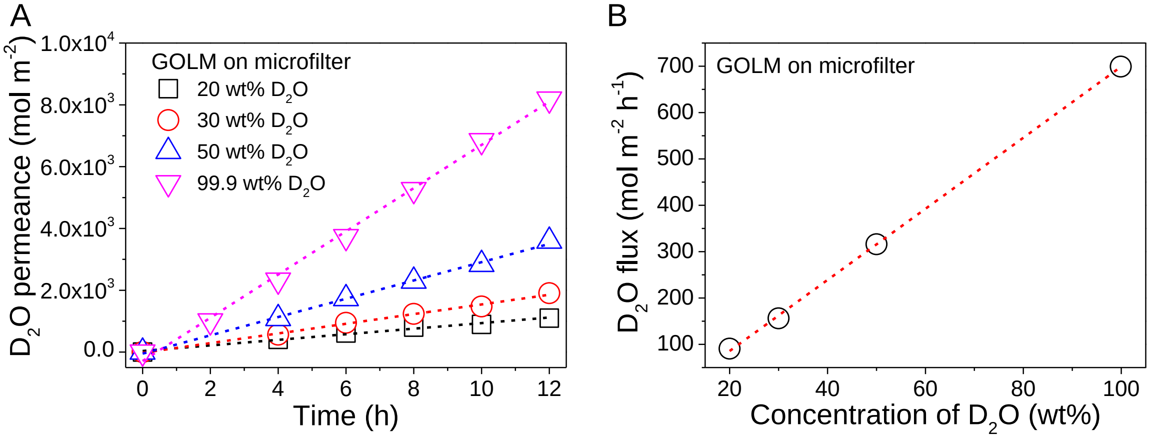

Fig. S6. (**A**) The permeations of D_2O with various feed concentrations through GOLM on microfilter. (**B**) D_2O fluxes as a function of feed concentration.

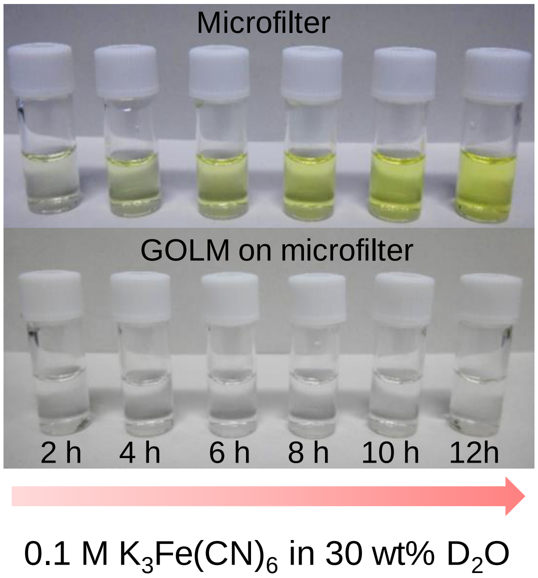

Fig. S7. Photographs showing the permeate solutions during the 12 h-long diffusions of 0.1 M $K_3Fe(CN)_6$ feed solution through microfilter and GOLM on microfilter, respectively.

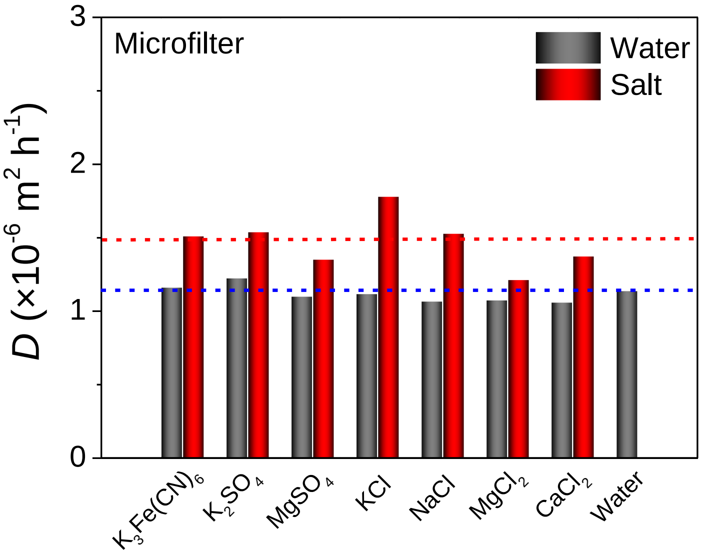

Fig. S8. Diffusivities of various salts and corresponding solvent water through microfilter.

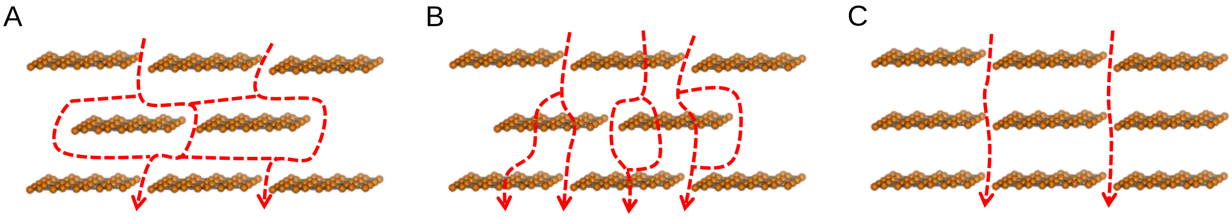

Fig. S9. Schematics of mass transport through the nanochannels within GOLM. (**A**) Neglecting the leakage through the nanopores on GO flakes. (**B**) Assuming the nanopores on GO flakes unblocked. (**C**) Assuming no turns in the nanochannels. (**B**) and (**C**) are two ideal cases that are impossible in reality.

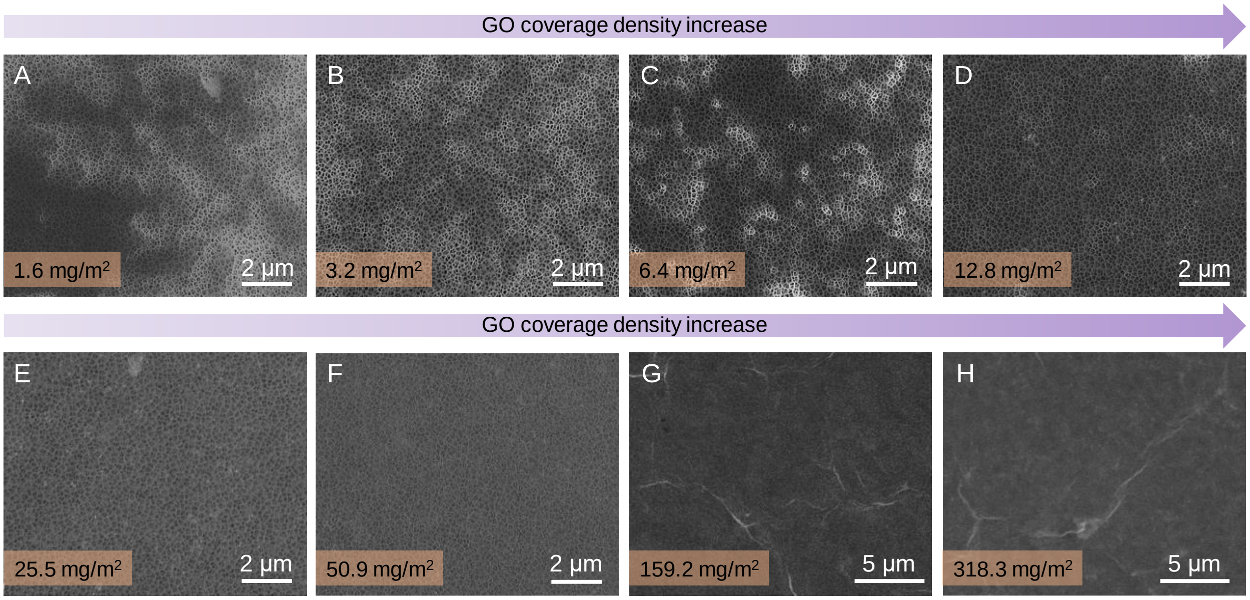

Fig. S10. Vacuum-assisted formation of GOLM on microfilter with increasing GO coverage density.

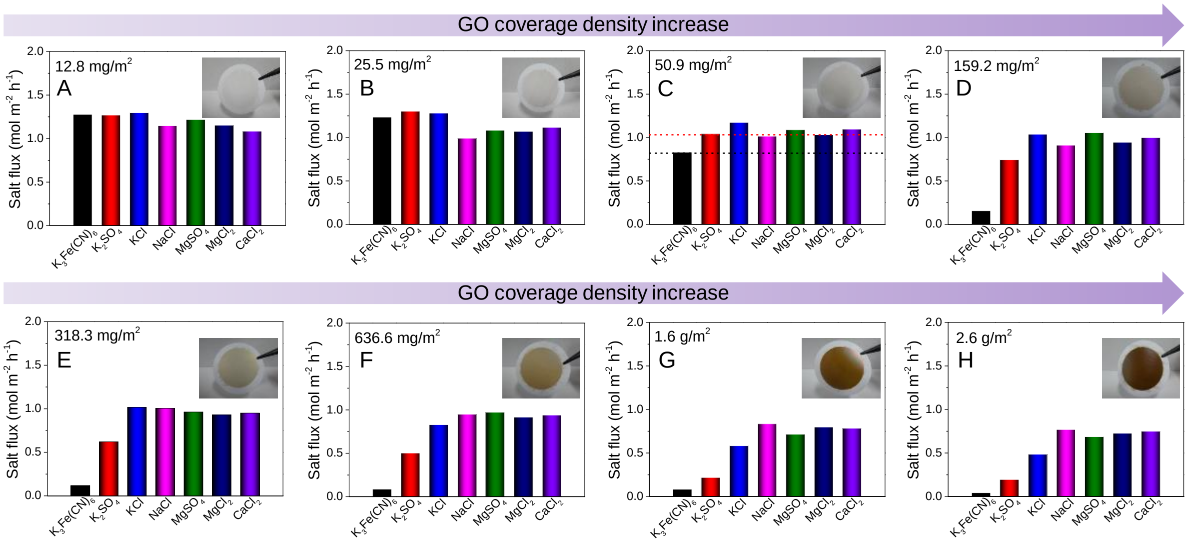

Fig. S11. The fluxes of various salts through GOLM on microfilter with increasing GO coverage density under the same concentration gradient (0.1 M) without considering the related water permeations.

4. References

1. W. S. Hummers, R. E. Offeman, Preparation of graphite oixde. *J. Am. Chem. Soc.* **80**, 1339–1339 (1958).
2. D. A. Dikin, S. Stankovich, E. J. Zimney, R. D. Piner, G. H. B. Dommett, G. Evmenenko, S. T. Nguyen, R. S. Ruoff, Preparation and characterization of graphene oxide paper. *Nature* **448**, 457–460 (2007).
3. S. Stankovich, D. A. Dikin, R. D. Piner, K. A. Kohlhaas, A. Kleinhammes, Y. Jia, Y. Wu, S. T. Nguyen, R. S. Ruoff, Synthesis of graphene-based nanosheets via chemical reduction of exfoliated graphite oxide. *Carbon* **45**, 1558–1565 (2007).
4. S. Park, R. S. Ruoff, Chemical methods for the production of graphenes, *Nat. Nanotechnol.* **4**, 217–224 (2009).
5. G. Eda, G. Fanchini, M. Chhowalla, Large-area ultrathin films of reduced graphene oxide as a transparent and flexible electronic material. *Nat. Nanotechnol.* **3**, 270–274 (2008).
6. C. Mattevi, G. Eda, S. Agnoli, S. Miller, K. A. Mkhoyan, O. Celik, D. Mastrogiovanni, G. Granozzi, E. Garfunkel, M. Chhowalla, Evolution of electrical, chemical, and structural properties of transparent and conducting chemically derived graphene thin films. *Adv. Funct. Mater.* **19**, 2577–2583 (2009).
7. C.-N. Yeh, K. Raidongia, J. Shao, Q.-H. Yang, J. Huang, On the origin of the stability of graphene oxide membranes in water. *Nat. Chem.* **7**, 166–170 (2015).
8. S. Kim, S. Zhou, Y. Hu, M. Acik, Y. J. Chabal, C. Berger, W. de Heer, A. Bongiorno and E. Riedo, Room-temperature metastability of multilayer graphene oxide films. *Nat. Mater.* **11**, 544–549 (2012).
9. D. R. Dreyer, S. Park, C. W. Bielawski, R. S. Ruoff, The chemistry of graphene oxide. *Chem. Soc. Rev.* **39**, 228–240 (2010).
10. S. Plimpton, Fast parallel algorithms for short-range molecular dynamics. *J. Comput. Phys.* **117**, 1–19 (1995).
11. C.-J. Shih, S. Lin, R. Sharma, M. S. Strano, D. Blankschtein, Understanding the pH-dependent behavior of graphene oxide aqueous solutions: A comparative experimental and molecular dynamics simulation study. *Langmuir* **28**, 235–241 (2012).
12. K. Falk, F. Sedlmeier, L. Joly, R. R. Netz, L. Bocquet, Molecular origin of fast water transport in carbon nanotube membranes: Superlubricity versus curvature dependent friction. *Nano Lett.* **10**, 4067–4073 (2010).
13. W. Xiong, J. Z. Liu, M. Ma, Z. Xu, J. Sheridan, Q. Zheng, Strain engineering water transport in graphene nanochannels. *Phys. Rev. E* **84**, 056329 (2011).
14. N. Wei, X. Peng, Z. Xu, Breakdown of fast water transport in graphene oxides. *Phys. Rev. E* **89**, 012113 (2014).
15. N. Wei, X. Peng, Z. Xu, Understanding water permeation in graphene oxide membranes. *ACS Appl. Mater. Interfaces* **6**, 5877–5883 (2014).
16. T. Werder, J. H. Walther, R. L. Jaffe, T. Halicioglu , P. Koumoutsakos, On the water-carbon interaction for use in molecular dynamics simulations of graphite and carbon nanotubes. *J.*

Phys. Chem. B **107**, 1345–1352 (2003).

17. D. Cohen-Tanugi, J. C. Grossman, Water desalination across nanoporous graphene. *Nano Lett.* **12**, 3602–3608 (2012).
18. R. W. Hockney, J. W. Eastwood, Computer simulation using particles. (McGraw-Hill, New York, 1981).
19. M. Lozada-Hidalgo, S. Hu, O. Marshall, A. Mishchenko, A. N. Grigorenko, R. A. W. Dryfe, B. Radha, I. V. Grigorieva, A. K. Geim, Sieving hydrogen isotopes through two-dimensional crystals. *Science* **351**, 68–70 (2016).
20. R. R. Nair, H. A. Wu, P. N. Jayaram, I. V. Grigorieva, A. K. Geim, Unimpeded permeation of water through helium-leak-tight graphene-based membranes. *Science* **335**, 442–444 (2012).
21. R. K. Joshi, P. Carbone, F. C. Wang, V. G. Kravets, Y. Su, I. V. Grigorieva, H. A. Wu, A. K. Geim, R. R. Nair, Precise and ultrafast molecular sieving through graphene oxide membranes. *Science* **343**, 752–754 (2014).
22. K. Erickson, R. Erni, Z. Lee, N. Alem, W. Gannett, A. Zettl, Determination of the local chemical structure of graphene oxide and reduced graphene oxide. *Adv. Mater.* **22**, 4467−4472 (2010).
23. D. Pacilé, J. C. Meyer, A. Fraile Rodríguez, M. Papagno, C. Gómez-Navarro, R. S. Sundaram, M. Burghard, K. Kern, C. Carbone, U. Kaiser, Electronic properties and atomic structure of graphene oxide membranes. *Carbon* **49**, 966−972 (2011).
24. C. Gomez-Navarro, J. C. Meyer, R. S. Sundaram, A. Chuvilin, S. Kurasch, M. Burghard, K. Kern, U. Kaiser, Atomic structure of reduced graphene oxide. *Nano Lett.* **10**, 1144−1148 (2010).
25. P. Sun, M. Zhu, K. Wang, M. Zhong, J. Wei, D. Wu, Z. Xu, H. Zhu, Selective ion penetration of graphene oxide membranes. *ACS Nano* **7**, 428–437 (2013).
26. P. Sun, F. Zheng, M. Zhu, Z. Song, K. Wang, M. Zhong, D. Wu, R. B. Little, Z. Xu, H. Zhu, Selective trans-membrane transport of alkali and alkaline earth cations through graphene oxide membranes based on cation-π interactions. *ACS Nano* **8**, 850–859 (2014).